The Cryosphere Discuss., 3, 1–31, 2009
www.the-cryosphere-discuss.net/3/1/2009/

The Cryosphere Discussions

The Cryosphere Discussions is the access reviewed discussion forum of *The Cryosphere*

A full-Stokes ice flow model for the vicinity of Dome Fuji, Antarctica, with induced anisotropy and fabric evolution

H. Seddik[1], **R. Greve**[1], **T. Zwinger**[2], **and L. Placidi**[3]

[1]Institute of Low Temperature Science, Hokkaido University, Kita-19, Nishi-8, Kita-ku, Sapporo 060-0819, Japan
[2]CSC – IT Center for Science Ltd., P.O. Box 405, 02101 Espoo, Finland
[3]Department of Structural and Geotechnical Engineering, "Sapienza" University of Rome, Via Eudossiana 18, 00184 Rome, Italy

Received: 29 October 2008 – Accepted: 17 November 2008 – Published: 19 January 2009

Correspondence to: H. Seddik (hakime@lowtem.hokudai.ac.jp)

Published by Copernicus Publications on behalf of the European Geosciences Union.

Abstract

A three-dimensional, thermo-mechanically coupled ice flow model with induced anisotropy has been applied to a ∼200×200 km domain around the Dome Fuji drill site, Antarctica. The model ("Elmer/Ice") is based on the open-source multi-physics package Elmer (http://www.csc.fi/elmer/) and solves the full-Stokes equations. Flow-induced anisotropy in ice is accounted for by an implementation of the *C*ontinuum-mechanical, *A*nisotropic *F*low model, based on an anisotropic *F*low *E*nhancement factor ("CAFFE model"). Steady-state simulations for present-day climate conditions are conducted. The main findings are: (i) the flow regime at Dome Fuji is a complex superposition of vertical compression, horizontal extension and bed-parallel shear; (ii) for a geothermal heat flux of 60 mW m^{-2} the basal temperature at Dome Fuji reaches the pressure melting point and the basal melting rate is ∼1 mm a^{-1}; (iii) the fabric shows a weak single maximum at Dome Fuji, which increases the age of the ice compared to an isotropic scenario; (iv) as a consequence of spatially variable basal melting conditions, and contrary to intuition, the basal age is smaller where the ice is thicker and larger where the ice is thinner. The latter result is of great relevance for the consideration of a future drill site in the area.

1 Introduction

Dome Fuji, situated at 77°19′01″ S, 39°42′12″ E, is the second-highest summit of the Antarctic ice sheet with an altitude of 3810 m a.s.l. (above mean sea level). Owing to its location on the Antarctic plateau (see Fig. 1) and the high elevation, it is one of the coldest places on Earth. Temperatures rarely rise above −30°C in summer and can drop to −80°C in winter. The annual average air temperature is −54.3°C (Watanabe et al., 2003). The climate is that of a cold desert, with very dry conditions and an annual precipitation of about 27 mm water equiv., which falls entirely as snow (Kameda et al., 2008).

Deep ice core drilling at Dome Fuji was started in August 1995, and in December 1996 a depth of 2503 m was reached. The core was recently dated by an innovative method based on the O_2/N_2 ratio of entrapped air (Kawamura et al., 2007), and covers a period back to ~340 ka. A second deep core was started in 2003. Drilling was carried out during four subsequent austral summers from 2003/2004 until 2006/2007, and by then a depth of 3035.22 m was reached. The drill did not hit the bedrock, but rock particles and refrozen water have been found in the deepest ice, indicating that the bedrock is close to the bottom of the borehole. This core was dated preliminarily by synchronizing the $\delta^{18}O$ profile with that of the Dome C ice core data from the European Project for Ice Coring in Antarctica (EPICA), for which an age scale was already constructed (Parrenin et al., 2007). As a result, the deepest parts of the second Dome Fuji ice core are estimated to be approximately 720 ka old, thus greatly extending the climatic record of the first core (Motoyama, 2007).

The surface and bedrock topographies within 30 km from the Dome Fuji drill site were measured with high spatial resolution and resampled to a 0.5-km grid (Fujita et al., 1999; Watanabe et al., 2003; S. Fujita, personal communication, 2006). According to these data, the surface topography is smooth and flat, surface elevations 30 km away from the drill site being only 7 to 30 m lower than at the drill site. The actual summit is located ~10 km west-north-west of the drill site and is ~1 m higher. The bedrock topography exhibits a pronounced subglacial trench running mainly from the north-east to the south-west, whereas higher ground dominates to the south-east and north-west of the drill site, which itself is situated on a flank. The difference between highest and lowest bedrock elevations in the area is more than 1000 m.

In this study, we apply the full-Stokes ice flow model Elmer/Ice to an extended ~200×200 km domain around Dome Fuji. The domain and the model equations, including the treatment of flow-induced anisotropy, are defined in Sect. 2. The numerical model itself is briefly introduced in Sect. 3. Section 4 constitutes the main focus of the study, where the simulation results for the ice flow, the anisotropic fabric, the temperature and the age are presented and discussed. Section 5 concludes the paper with the

discussion of some caveats and consequences for the consideration of another drill site in the region.

2 Full-Stokes flow problem with anisotropy

2.1 Coordinate system and domain

The vicinity of Dome Fuji is projected to a polar stereographic map with standard parallel at 77°19′01″ S (the latitude of Dome Fuji) and central meridian at 0° E. In the stereographic plane, we set up a Cartesian coordinate system with the south pole as origin. The horizontal plane is spanned by x and y, aligned with the natural x- and y-directions in Fig. 1, and z points upward. The associated unity vectors are $\boldsymbol{e}_x$, $\boldsymbol{e}_y$ and $\boldsymbol{e}_z$, respectively.

We define a quadratic domain of the size 203.092×203.092 km around Dome Fuji (Fig. 1), which corresponds to a 200×200 km domain in the stereographic plane with standard parallel at 71° S used by the Antarctica version of the large-scale ice-sheet model SICOPOLIS (Greve, 2006). Within 30 km from Dome Fuji, the surface and bedrock topographies are given by the high-resolution data mentioned in the introduction. Outside this area, they are defined by the 20-km SICOPOLIS grid, based on resamplings of the RAMPDEM V2 (Liu et al., 2001) and BEDMAP (Lythe et al., 2000) data-sets, respectively. We do not consider any evolution of the surface and bedrock topographies, but only deal with the present-day geometry. The topographies are shown in Figs. 2 and 3.

2.2 Dynamic/thermodynamic model equations

2.2.1 Field equations

For the flow of ice sheets, the acceleration (inertia force) is negligible, so that the equation of motion is given by the Stokes equation

$$-\operatorname{grad} p + \eta \nabla^2 \boldsymbol{v} + (\operatorname{grad} \boldsymbol{v} + (\operatorname{grad} \boldsymbol{v})^{\mathrm{T}}) \cdot \operatorname{grad} \eta + \rho \boldsymbol{g} = \boldsymbol{0}, \quad (1)$$

where p is the pressure, η is the viscosity, $\boldsymbol{v}$ is the velocity vector, ρ is the ice density and $\boldsymbol{g}=-g\boldsymbol{e}_z$ is the gravity acceleration vector pointing downward (for values see Table 1). The viscosity is described by the CAFFE flow law,

$$\eta = \frac{1}{2}[\hat{E}(\mathcal{A})]^{-1/n}[A(T')]^{-1/n} d^{-(1-1/n)}, \quad (2)$$

where $\hat{E}(\mathcal{A})$ is the anisotropic enhancement factor (see below, Sect. 2.3), $A(T')$ is the rate factor, $d=\sqrt{\frac{1}{2}\mathrm{tr}(\mathrm{D}^2)}$ is the effective strain rate and n is the power-law exponent. The rate factor depends on the temperature relative to pressure melting $T'=T-T_m$ (T: absolute temperature, $T_m=T_0-\beta p$: pressure melting point, T_0: melting point at zero pressure, β: Clausius-Clapeyron constant) via the Arrhenius law given in Table 1. The tensor $\mathrm{D}=\operatorname{sym}\mathrm{L}=\frac{1}{2}(\mathrm{L}+\mathrm{L}^{\mathrm{T}})$ is the strain-rate tensor (symmetric part of the velocity gradient $\mathrm{L}=\operatorname{grad}\boldsymbol{v}$).

Since ice is an (almost) incompressible material, the mass balance simply states that the velocity field is solenoidal,

$$\operatorname{div}\boldsymbol{v}=0. \quad (3)$$

The temperature equation follows from the general balance equation of internal energy and reads

$$\rho c(T)\left(\frac{\partial T}{\partial t} + \boldsymbol{v}\cdot\operatorname{grad} T\right) = \operatorname{div}(\kappa(T)\operatorname{grad} T) + 4\eta d^2, \quad (4)$$

where κ and c are the heat conductivity and specific heat of ice, respectively (Table 1).

The age equation states that the age of ice, A, is equal to the elapsed time since an ice particle settled on the surface as a snowflake. This yields in a spatially fixed frame of reference the expression

$$\frac{\partial A}{\partial t} + \boldsymbol{v} \cdot \operatorname{grad} A = 1, \tag{5}$$

which described a purely advective transport.

2.2.2 Boundary conditions

In order to provide a closed system, the above field equations need to be complemented by suitable boundary conditions. The ice surface is assumed to be stress-free (atmospheric pressure and wind stress neglected), the surface temperature T_s is prescribed (Table 1) and the age of ice at the surface is equal to zero. At the base, no-slip conditions are assumed to prevail, the geothermal heat flux q_{geo} is prescribed (Table 1), and the basal melting rate is computed by solving the energy jump condition. At the lateral boundaries of the domain, shallow-ice stresses are prescribed, and the temperature gradient is assumed to vanish (zero-flux condition). For more details see Seddik (2008).

2.3 CAFFE model

In order to take into account flow-induced anisotropy, we use the *C*ontinuum-mechanical, *A*nisotropic *F*low model, based on an anisotropic *F*low *E*nhancement factor ("CAFFE model"), which is explained in detail in the studies by Placidi et al. (2008) and Greve et al. (2008), and was already applied by Seddik et al. (2008) to the ice column of the EDML ice core in the Atlantic sector of East Antarctica. The polycrystal deformability $\mathcal{A}$ is defined as

$$\mathcal{A} = 5 \int_{S^2} \frac{(\mathrm{S} \cdot \boldsymbol{n})^2 - (\boldsymbol{n} \cdot \mathrm{S} \cdot \boldsymbol{n})^2}{\operatorname{tr}(\mathrm{S}^2)} f^\star(\boldsymbol{n}) \, \mathrm{d}^2 n = 5 \int_{S^2} \frac{(\mathrm{D} \cdot \boldsymbol{n})^2 - (\boldsymbol{n} \cdot \mathrm{D} \cdot \boldsymbol{n})^2}{\operatorname{tr}(\mathrm{D}^2)} f^\star(\boldsymbol{n}) \, \mathrm{d}^2 n, \tag{6}$$

where S^2 is the unit sphere, S is the deviatoric stress tensor, $\boldsymbol{n}$ is the orientation (normal unit vector of the basal plane, direction of the c-axis) and $f^\star(\boldsymbol{n})$ is the orientation distribution function (ODF). The latter is defined as

$$f^\star(\boldsymbol{n}) = \frac{\rho^\star(\boldsymbol{n})}{\rho}, \tag{7}$$

where $\rho^\star(\boldsymbol{n})$ is the orientation mass density (OMD), that is, the mass per volume and orientation. By introducing the second- and fourth-order orientation tensors,

$$\begin{aligned} \mathrm{a}^{(2)} &= \int_{S^2} (\boldsymbol{n}\,\boldsymbol{n}) f^\star(\boldsymbol{n})\,\mathrm{d}^2 n, \\ \mathrm{a}^{(4)} &= \int_{S^2} (\boldsymbol{n}\,\boldsymbol{n}\,\boldsymbol{n}\,\boldsymbol{n}) f^\star(\boldsymbol{n})\,\mathrm{d}^2 n, \end{aligned} \tag{8}$$

the polycrystal deformability Eq. (6) can be expressed as

$$\mathcal{A} = \frac{5}{\mathrm{tr}(\mathrm{S}^2)}\left[(\mathrm{S}\cdot\mathrm{a}^{(2)}) : \mathrm{S} - (\mathrm{a}^{(4)} : \mathrm{S}) : \mathrm{S}\right] = \frac{5}{\mathrm{tr}(\mathrm{D}^2)}\left[(\mathrm{D}\cdot\mathrm{a}^{(2)}) : \mathrm{D} - (\mathrm{a}^{(4)} : \mathrm{D}) : \mathrm{D}\right]. \tag{9}$$

The anisotropic enhancement factor $\hat{E}(\mathcal{A})$ depends on the polycrystal deformability by the smooth, monotonically increasing function

$$\hat{E}(\mathcal{A}) = \begin{cases} E_{\min} + (1 - E_{\min})\mathcal{A}^t, \quad t = \dfrac{8}{21}\dfrac{E_{\max} - 1}{1 - E_{\min}}, & 0 \le \mathcal{A} \le 1, \\ \dfrac{4\mathcal{A}^2(E_{\max} - 1) + 25 - 4E_{\max}}{21}, & 1 \le \mathcal{A} \le \dfrac{5}{2}, \end{cases} \tag{10}$$

with the two parameters $E_{\max}$=10 (maximum softening) and $E_{\min}$=0.1 (maximum hardening). The function is illustrated in Fig. 4.

The evolution equation for the OMD is the orientation mass balance

$$\frac{\partial \rho^\star}{\partial t} + \mathrm{div}(\rho^\star \boldsymbol{v}) + \mathrm{div}_{S^2}(\rho^\star \boldsymbol{u}^\star + \boldsymbol{q}^\star) = \rho^\star \Gamma^\star. \tag{11}$$

In this equation, div is the normal, three-dimensional divergence operator, div_{S^2} the divergence operator on the unit sphere, $\boldsymbol{u}^\star(\boldsymbol{n})$ the orientation transition rate, $\boldsymbol{q}^\star(\boldsymbol{n})$ the orientation flux and $\Gamma^\star(\boldsymbol{n})$ the orientation production rate. Physically, the orientation transition rate corresponds to grain rotation, the orientation flux to rotation recrystallization (polygonization), and the orientation production rate to migration recrystallization. Like in the study by Seddik et al. (2008), we shall not take into account recrystallization processes here, and thus set $\boldsymbol{q}^\star(\boldsymbol{n})=\mathbf{0}$, $\Gamma^\star(\boldsymbol{n}) = 0$. This leaves the orientation transition rate to be determined, for which the constitutive equation

$$\boldsymbol{u}^\star = \iota \cdot [(\boldsymbol{n} \cdot \mathrm{D} \cdot \boldsymbol{n})\boldsymbol{n} - \mathrm{D} \cdot \boldsymbol{n}] + \mathrm{W} \cdot \boldsymbol{n} \tag{12}$$

is employed. The parameter ι is a positive constant. The additional term $\mathrm{W}\cdot\boldsymbol{n}$ with the spin tensor $\mathrm{W}=\mathrm{skw}\,\mathrm{L}=\frac{1}{2}(\mathrm{L}-\mathrm{L}^{\mathrm{T}})$ (skew-symmetric part of the velocity gradient L) describes the contribution of local rigid-body rotations.

For a spatially three-dimensional problem, the evolution Eq. (11) is six-dimensional (three spatial directions, time, two orientation components), which renders its numerical solution on a reasonably fine grid unfeasible. Therefore, we resolve to a simplified formulation with the orientation tensors introduced above. By differentiating Eq. $(8)_1$ with respect to time and inserting the constitutive Eq. (12), one obtains an evolution equation for the second-order orientation tensor,

$$\frac{\partial \mathrm{a}^{(2)}}{\partial t} + \mathrm{grad}\,\mathrm{a}^{(2)} \cdot \boldsymbol{v} = \mathrm{W} \cdot \mathrm{a}^{(2)} - \mathrm{a}^{(2)} \cdot \mathrm{W} - \iota[(\mathrm{D} \cdot \mathrm{a}^{(2)} + \mathrm{a}^{(2)} \cdot \mathrm{D}) - 2\mathrm{a}^{(4)} : \mathrm{D}] \tag{13}$$

(for the detailed derivation see Seddik, 2008). Evidently, this equation contains the unknown fourth-order orientation tensor $\mathrm{a}^{(4)}$ on the right-hand side. For the latter, we formulate a closure condition of the form

$$\mathrm{a}^{(4)} = \mathrm{F}_{\mathrm{IBOF}}(\mathrm{a}^{(2)}), \tag{14}$$

that is, we relate $\mathrm{a}^{(4)}$ by some non-linear function $\mathrm{F}_{\mathrm{IBOF}}$ to $\mathrm{a}^{(2)}$. Specifically, following Gillet-Chaulet (2006) and Gillet-Chaulet et al. (2006), we adopt the invariant-based

optimal fitting closure approximation (IBOF) proposed by Chung and Kwon (2002) because of its physical accuracy and numerical stability compared to previously proposed closure functions. The exact form of the very lengthy function F_{IBOF} shall not be given here; we refer the reader to Seddik (2008) instead. The boundary condition for Eq. (13) is isotropy at the ice surface, that is, $a^{(2)}$ is set to $I/3$ (where I is the identity tensor).

3 Finite-element model Elmer/Ice

The model equations detailed in Sects. 2.2 and 2.3 are solved numerically with the model Elmer/Ice, which is based on the open-source multi-physics package Elmer provided by the CSC – IT Center for Science Ltd. in Espoo, Finland (see http://www.csc.fi/elmer/), and uses the finite-element method (FEM). The solution technique is similar to the one explained in the study by Zwinger et al. (2007) in the context of an application of Elmer/Ice to a small crater glacier. In particular, we only consider steady-state scenarios with present-day climatic forcing and fixed geometry. Differences are that we are concerned with incompressible ice instead of compressible firn, and that we take into account flow-induced anisotropy by the CAFFE model. For more details on the numerical solution strategy see Seddik (2008).

Using the commercial pre-processing tool Gambit, a mesh of the computational domain defined in Sect. 2.1 has been created. The mesh has a rather coarse resolution of 7 km near the boundaries, which refines up to 0.5 km towards the center of the domain, located very close to (~0.23 km away from) the position of Dome Fuji. An inner square domain (6×6 km) is meshed with mapped elements with a resolution of 0.5 km. This domain is surrounded by a second square domain (60×60 km) meshed with mapped elements using a 6-km resolution. The connection between those two square sub-domains is performed with a refining resolution towards the inner square. In order to connect the outer square to the domain boundaries, four sub-domains have been created and meshed with paved elements. The vertical direction is discretized by 20 equidistant layers. The resulting mesh contains 5406 bilinear quadrilateral elements,

30860 trilinear brick elements and a total of 33642 nodes (Fig. 5).

4 Simulations for the vicinity of Dome Fuji

4.1 Anisotropic steady-state simulation

We will now discuss the results of a present-day steady-state run for the 203.092 × 203.092 km domain around Dome Fuji as described in Sects. 2, 3 and Table 1. The geothermal heat flux of 60 mW m^{-2} was chosen in order to produce a basal melting rate of ∼1 mm a^{-1} at the Dome Fuji drill site, which, by application of the analytical formula given by Greve et al. (2002) for the one-dimensional steady-state problem with Dansgaard-Johnsen type vertical strain, leads to a basal age of ∼700 ka (close to the estimate of 720 ka reported by Motoyama, 2007). In order to prevent the basal age from becoming infinite in regions where the basal temperature is below the pressure melting point and the ice is frozen to the ground, a basal-melting offset of 0.1 mm a^{-1} is applied there.

Figure 6 shows the simulated surface velocity for the entire domain. The ice flow points away from the summit, follows largely the direction of the steepest surface slope despite the pronounced relief of the bedrock (Figs. 2 and 3) and reaches maximum speeds of ∼1.4 m a^{-1} around the margin of the domain. Within 30 km from Dome Fuji, typical values are of the order of 0.1 m a^{-1}. This is consistent with average values of 0.16 m a^{-1} at Dome Fuji Station and 0.11 m a^{-1} at Station DF80 (∼6 km further south-south-west) measured between January 1994 and January 2004 (Dome Fuji)/December 2003 (DF80) (Motoyama et al., 2008).

The strain rates at the Dome Fuji drill site shown in Fig. 7 are very small (of the order of 10^{-5} a^{-1}), which reflects the fact that the drill site is only ∼10 km away from the actual summit position. The flow regime at the drill site is a complex superposition of vertical compression (D_{zz}), horizontal extension (mainly D_{xx}) and bed-parallel shear (D_{xz}, D_{yz}). As expected, vertical compression and horizontal extension dominate in the

upper parts of the ice column, whereas bed-parallel shear becomes more important in the lower parts.

The largest eigenvalue a_3 (that corresponds approximately to the vertical direction) of the second-order orientation tensor $a^{(2)}$ near the ice base (at 95% depth), which is shown in Fig. 8, measures the anisotropy of the simulated fabric. A value of 1/3 means isotropy, whereas a value of 1 corresponds to an ideal single-maximum fabric (perfect alignment of all *c*-axes). Generally, we find values of about 0.5, which denote weakly anisotropic fabrics, in agreement with the small strain rates in the model domain that forbid the formation of stronger anisotropy. In the areas farthest away from the summit where stronger bed-parallel shear prevails, the values of a_3 tend to increase slightly.

Directly at the drill site, Fig. 9 shows the anisotropic fabric expressed as the smallest (a_1), middle (a_2) and largest (a_3) eigenvalue of $a^{(2)}$ over depth. The anisotropy manifests itself mainly by values of a_3 clearly larger than and values of a_1 clearly smaller than 1/3, whereas a_2 is only slightly smaller than 1/3 over the whole profile. This means that elongated single-maximum fabrics are at hand, which is consistent with the the strong dominance of the horizontal extension component D_{xx} over D_{yy} (Fig. 7). It is also interesting to note that, starting from isotropic conditions at the surface, anisotropy develops down to ∼800 m depth, stays rather constant further down to ∼2500 m depth, and increases again in the bottom-most ∼500 m. The latter is probably related to the stronger influence of bed-parallel shear at large depths.

The simulated basal temperature is depicted in Fig. 10. More than half of the basal ice in the domain is at the pressure melting point, including the Dome Fuji drill site itself. These areas are characterized by large ice thicknesses, whereas lower basal temperatures (down to ∼−10°C) occur in areas where the ice is relatively thin due to higher bedrock elevations (Fig. 3). While this is the expected behaviour, it has a surprising consequence for the distribution of the basal age.

Figure 11 shows the simulated age at 95% depth for the entire model domain. At the Dome Fuji drill site, its value is ∼450 ka and increases to ∼850 ka directly at the base. This is somewhat higher than the estimated real value of 720 ka (Motoyama, 2007). Of

course, our results are biased by the simplifying steady-state assumption, and we do not aim at providing an accurate dating in terms of absolute values. However, the *distribution* of the age is less affected by this assumption and should be reasonable. One would expect intuitively that the near-basal age increases with increasing ice thickness (lower bedrock elevation); however, a comparison of Figs. 3 and 11 shows that this is not the case. While the age at 95% varies significantly in the domain, the relation to the ice thickness is not evident at first glance. The scatter plots shown in Fig. 12 reveal that the correlation is only slightly positive at 95% depth and even strongly negative at the base; that is, the basal age tends to decrease with increasing ice thickness (note that Fig. 12b shows only the results for warm-based areas because of the above-mentioned problem with ill-defined ages in case of a cold base). The reason for this surprising behaviour is that basal melting increases with increasing ice thickness ($\sim$1 mm a^{-1} at the Dome Fuji drill site), which melts away the oldest ice.

4.2 Comparison with an isotropic simulation

In order to investigate the influence of the flow-induced anisotropic fabric, we have also conducted a present-day steady-state simulation with the fabric evolution "switched off" and the enhancement factor uniformly set to $E=1$ instead. The resulting surface velocity distribution of this isotropic simulation turns out to be very similar to that of the anisotropic simulation shown in Fig. 6, and it shall therefore not be shown separately. By contrast, the age of the ice is more affected, the anisotropic simulation producing generally larger ages than the isotropic simulation. This is illustrated in Fig. 13, which depicts the age profiles at Dome Fuji for both simulations. At the base, a value of $\sim$700 ka from the isotropic simulation contrasts with $\sim$850 ka from the anisotropic simulation. The reason for this behaviour is that the weak single-maximum fabric at the drill site (Fig. 9) is unfavourable for vertical compression, so that vertical strain rates and velocities in the anisotropic simulation are slightly smaller than in the isotropic simulation.

It is also interesting to note that the slightly positive correlation between the age at

95% depth and the ice thickness, as well as the strongly negative one between the basal age and the ice thickness, observed above (Fig. 12) are robust features and show up also in the isotropic simulation (Fig. 14). The slopes of the corresponding regression lines are somewhat smaller in the isotropic case, which demonstrates the non-negligible effect of anisotropy on age; however, basal melting limits efficiently the age of the basal ice for large thicknesses irrespective of the consideration or non-consideration of anisotropy.

5 Discussion and conclusion

Some caveats to the results presented above must be noted. In addition to the steady-state approach and the applied basal-melting offset for cold-based ice, a source of uncertainty is the assumption that the geothermal heat flux is spatially constant. Even for a rather small area like our ~200×200 km domain this is not necessarily the case, and if there is considerable spatial variability, the distributions of the basal temperature, melting rate and age will be affected.

In this context, it is interesting to note that the layer inclination of the Dome Fuji ice core shows sudden increases at several depths and reaches ~50° near the bottom (Dome Fuji Ice Core Project community paper, in preparation). This can be explained partly by the contrast between cold-based ice (no basal melting) and temperate-based ice (basal melting) in the immediate vicinity of the drill site found in our simulations (Fig. 10). However, the extreme layer inclination near the bottom and especially the discontinuous increase with depth probably require additional mechanisms. One possibility is that the spatial distribution of the geothermal heat flux has experienced abrupt changes at several occasions. Alternatively, episodic drainage of a nearby subglacial lake, as discussed in a recent study by Pattyn (2008), may be responsible for the irregular layer inclination.

Preliminary data by Miyamoto (personal communication, 2008) indicate that the real fabric of the Dome Fuji ice core develops a somewhat stronger single-maximum fabric

with depth than that of our simulations, especially at large depths. This discrepancy is most likely due to the disregard of migration recrystallization in the model, as it was already pointed out in the study by Seddik et al. (2008) on the EDML ice core.

All of these conjectured mechanisms can alter the distribution of the age of the ice in the region. Furthermore, the old ice predicted by our simulations for rather thin locations suffers from strong layer thinning, which is less pronounced for the younger ice at thicker locations. With regard to the idea of retrieving another deep ice core in the vicinity of Dome Fuji, this is important to consider because the temporal resolution of the oldest, near-basal ice would be quite poor. An area-wide radio-echo-sounding survey would be desirable in order to obtain more information about the detailed conditions in the region.

Acknowledgements. This study is based on the doctoral thesis by Seddik (2008). The authors wish to thank T. Hondoh, M. Ikeda, T. Shiraiwa (Hokkaido University, Sapporo, Japan) and A. Abe-Ouchi (Center for Climate System Research, Tokyo, Japan) for co-supervising the thesis. O. Gagliardini and F. Gillet-Chaulet (Laboratory of Glaciology and Environmental Geophysics LGGE, Grenoble, France) have contributed considerably to the development and numerical implementation of the CAFFE model, in particular with regard to the IBOF closure approximation. The work was supported by a Grant-in-Aid for Scientific Research (No. 18340135) from the Japan Society for the Promotion of Science, and by a Grant-in-Aid for Creative Scientific Research (No. 14GS0202) from the Japanese Ministry of Education, Culture, Sports, Science and Technology.

References

Chung, D. H. and Kwon, T. H.: Invariant-based optimal fitting closure approximation for the numerical prediction of flow-induced fiber orientation, J. Rheol., 46, 169–194, 2002. 9

Fujita, S., Maeno, H., Uratsuka, S., Furukawa, T., Mae, S., Fujii, Y., and Watanabe, O.: Nature of radio-echo layering in the Antarctic ice sheet detected by a two-frequency experiment, J. Geophys. Res., 104, 13 013–13 024, 1999. 3

Gillet-Chaulet, F.: Modélisation de l'écoulement de la glace polaire anisotrope et premières

applications au forage de Dôme C, Doctoral thesis, Joseph Fourier University, Grenoble, France, 2006. 8

Gillet-Chaulet, F., Gagliardini, O., Meyssonnier, J., Zwinger, T., and Ruokolainen, J.: Flow-induced anisotropy in polar ice and related ice-sheet flow modelling, J. Non-Newton. Fluid Mech., 134, 33–43, 2006. 8

Greve, R.: Large-scale simulation of the Antarctic ice sheet over climate cycles, Presentation, Ice-Core-Consortium/Dating-Research-Consortium Meeting, National Institute of Polar Research, Tokyo, Japan, 26–27 October 2006, http://hdl.handle.net/2115/34433, Hokkaido University Collection of Scholarly and Academic Papers (HUSCAP), 2006. 4

Greve, R., Wang, Y., and Mügge, B.: Comparison of numerical schemes for the solution of the advective age equation in ice sheets, Ann. Glaciol., 35, 487–494, 2002. 10

Greve, R., Placidi, L., and Seddik, H.: A continuum-mechanical model for the flow of anisotropic polar ice, in: Proceedings of the 2nd International Workshop on Physics of Ice Core Records (PICR-2), edited by Hondoh, T., Institute of Low Temperature Science, Hokkaido University, Sapporo, Japan, in press, 2009. 6

Kameda, T., Motoyama, H., Fujita, S., and Takahashi, S.: Temporal and spatial variability of surface mass balance at Dome Fuji, East Antarctica, by the stake method from 1995 to 2006, J. Glaciol., 54, 107–116, 2008. 2

Kawamura, K., Parrenin, F., Lisiecki, L., Uemura, R., Vimeux, F., Severinghaus, J. P., Hutterli, M. A., Nakazawa, T., Aoki, S., Jouzel, J., Raymo, M. E., Matsumoto, K., Nakata, H., Motoyama, H., Fujita, S., Goto-Azuma, K., Fujii, Y., and Watanabe, O.: Northern Hemisphere forcing of climatic cycles in Antarctica over the past 360,000 years, Nature, 448, 912–916, doi:10.1038/nature06015, 2007. 3

Liu, H., Jezek, K., Li, B., and Zhao, Z.: Radarsat Antarctic Mapping Project digital elevation model version 2, Digital media, National Snow and Ice Data Center, Boulder, CO, USA, 2001. 4

Lythe, M. B., Vaughan, D. G., and the BEDMAP Consortium: BEDMAP – bed topography of the Antarctic, 1:10 000 000 scale map, BAS (Misc) 9, Cambridge, British Antarctic Survey, 2000. 4

Motoyama, H.: The second deep ice coring project at Dome Fuji, Antarctica, Sci. Drill., 5, 41–43, doi:10.2204/iodp.sd.5.05.2007, 2007. 3, 10, 11

Motoyama, H., Furukawa, T., and Nishio, F.: Study of ice flow observations in Shirase drainage basin and around Dome Fuji area, East Antarctica, by differential GPS method, Nankyoku

Shiryō (Antarctic Record), 52, 216–231, written in Japanese with English summary, 2008. 10

Parrenin, F., Barnola, J.-M., Beer, J., Blunier, T., Castellano, E., Chappellaz, J., Dreyfus, G., Fischer, H., Fujita, S., Jouzel, J., Kawamura, K., Lemieux-Dudon, B., Loulergue, L., Masson-Delmotte, V., Narcisi, B., Petit, J.-R., Raisbeck, G., Raynaud, D., Ruth, U., Schwander, J., Severi, M., Spahni, R., Steffensen, J. P., Svensson, A., Udisti, R., Waelbroeck, C., and Wolff, E.: The EDC3 chronology for the EPICA Dome C ice core, Clim. Past, 3, 485–497, 2007, http://www.clim-past.net/3/485/2007/. 3

Pattyn, F.: Investigating the stability of subglacial lakes with a full Stokes ice-sheet model, J. Glaciol., 54, 353–361, 2008. 13

Placidi, L., Greve, R., Seddik, H., and Faria, S. H.: Continuum-mechanical, anisotropic flow model, based on an anisotropic flow enhancement factor (CAFFE), Continuum Mech. Therm., submitted, 2008. 6

Seddik, H.: A full-Stokes finite-element model for the vicinity of Dome Fuji with flow-induced ice anisotropy and fabric evolution, Doctoral thesis, Graduate School of Environmental Science, Hokkaido University, Sapporo, Japan, http://hdl.handle.net/2115/34136, Hokkaido University Collection of Scholarly and Academic Papers (HUSCAP), 2008. 6, 8, 9, 14

Seddik, H., Greve, R., Placidi, L., Hamann, I., and Gagliardini, O.: Application of a continuum-mechanical model for the flow of anisotropic polar ice to the EDML core, Antarctica, J. Glaciol., 54, 631–642, 2008. 6, 8, 14

Watanabe, O., Kamiyama, K., Motoyama, H., Fujii, Y., Igarashi, M., Furukawa, T., Goto-Azuma, K., Saito, T., Kanamori, S., Kanamori, N., Yoshida, N., and Uemura, R.: General tendencies of stable isotopes and major chemical constituents of the Dome Fuji deep ice core, in: Global Scale Climate and Environment Study through Polar Deep Ice Cores, edited by Shoji, H. and Watanabe, O., pp. 1–24, National Institute of Polar Research, Tokyo, Japan, 2003. 2, 3

Zwinger, T., Greve, R., Gagliardini, O., Shiraiwa, T., and Lyly, M.: A full Stokes-flow thermo-mechanical model for firn and ice applied to the Gorshkov crater glacier, Kamchatka, Ann. Glaciol., 45, 29–37, 2007. 9

Table 1. Standard physical parameters and boundary conditions used in this study.

Quantity	Value
Density of ice, ρ	$910\,\mathrm{kg\,m^{-3}}$
Gravity acceleration, g	$9.81\,\mathrm{m\,s^{-2}}$
Power-law exponent, n	3
Rate factor, $A(T')$	$A_0 \mathrm{e}^{-Q/R(T_0+T')}$
Pre-exponential constant, A_0	$3.985\times10^{-13}\,\mathrm{s^{-1}\,Pa^{-3}}$ $(T'\leq-10^{\circ}\mathrm{C})$ $1.916\times10^{3}\,\mathrm{s^{-1}\,Pa^{-3}}$ $(T'\geq-10^{\circ}\mathrm{C})$
Activation energy, Q	$60\,\mathrm{kJ\,mol^{-1}}$ $(T'\leq-10^{\circ}\mathrm{C})$ $139\,\mathrm{kJ\,mol^{-1}}$ $(T'\geq-10^{\circ}\mathrm{C})$
Melting temperature at low pressure, T_0	273.16 K
Clausius-Clapeyron constant, β	$9.8\times10^{-8}\,\mathrm{K\,Pa^{-1}}$
Universal gas constant, R	$8.314\,\mathrm{J\,mol^{-1}K^{-1}}$
Heat conductivity of ice, κ	$9.828\mathrm{e}^{-0.0057T[\mathrm{K}]}\,\mathrm{W\,m^{-1}K^{-1}}$
Specific heat of ice, c	$(146.3 + 7.253T[\mathrm{K}])\,\mathrm{J\,kg^{-1}K^{-1}}$
Latent heat of ice, L	$3.35\times10^{5}\,\mathrm{J\,kg^{-1}}$
Surface temperature, T_s	$-54.3^{\circ}\mathrm{C}$
Geothermal heat flux, q_{geo}	$60\,\mathrm{mW\,m^{-2}}$
Basal sliding velocity, v_b	0 (no-slip)
Orientation transition parameter, ι	0.6
Length of year, 1 a	31 556 926 s

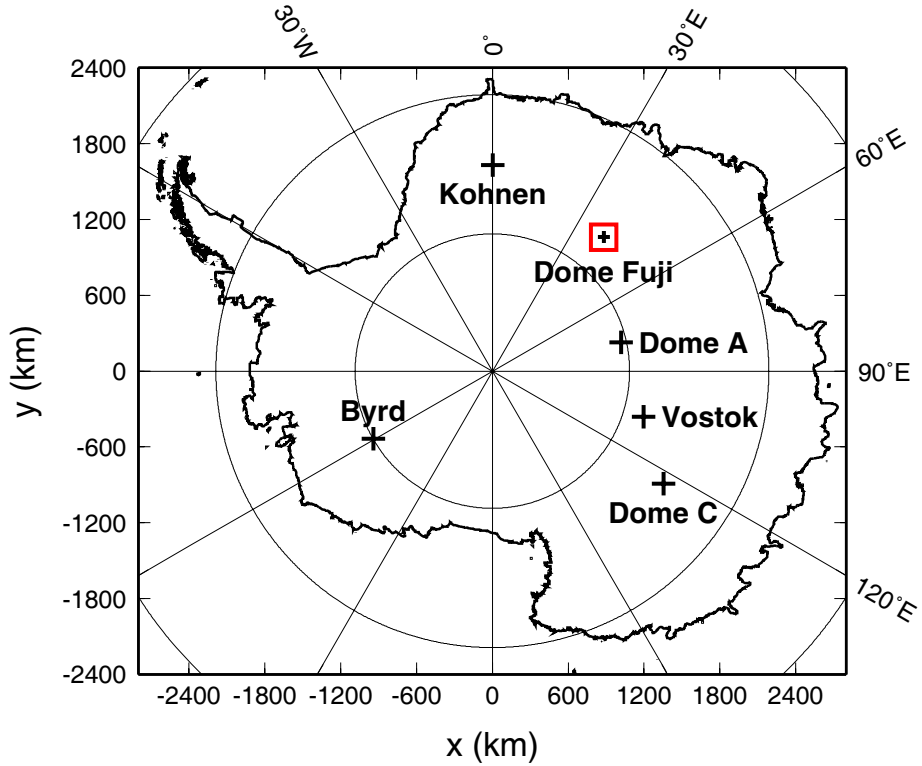

Fig. 1. The Antarctic ice sheet (with ice shelves), and the locations of the drill sites Dome Fuji, Vostok, Dome A, Dome C, Kohnen and Byrd. The red square around Dome Fuji represents the 203.092×203.092 km domain which is modelled in this study.

TCD
3, 1–31, 2009

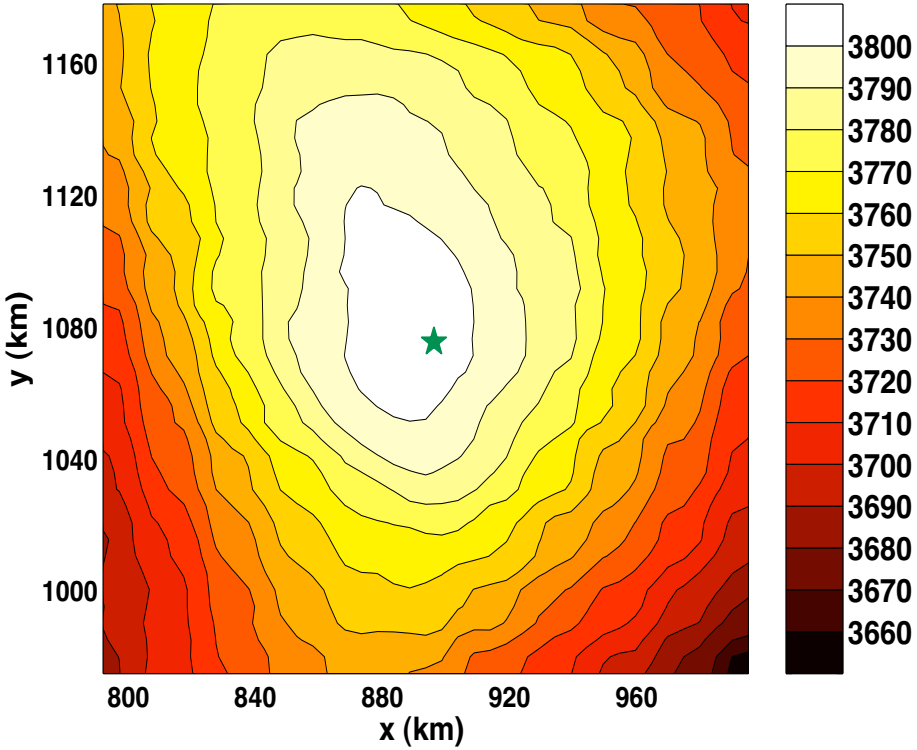

Fig. 2. Surface topography in the model domain (in m a.s.l., contour spacing 10 m). The green star indicates the location of the Dome Fuji drill site, north is towards the top right.

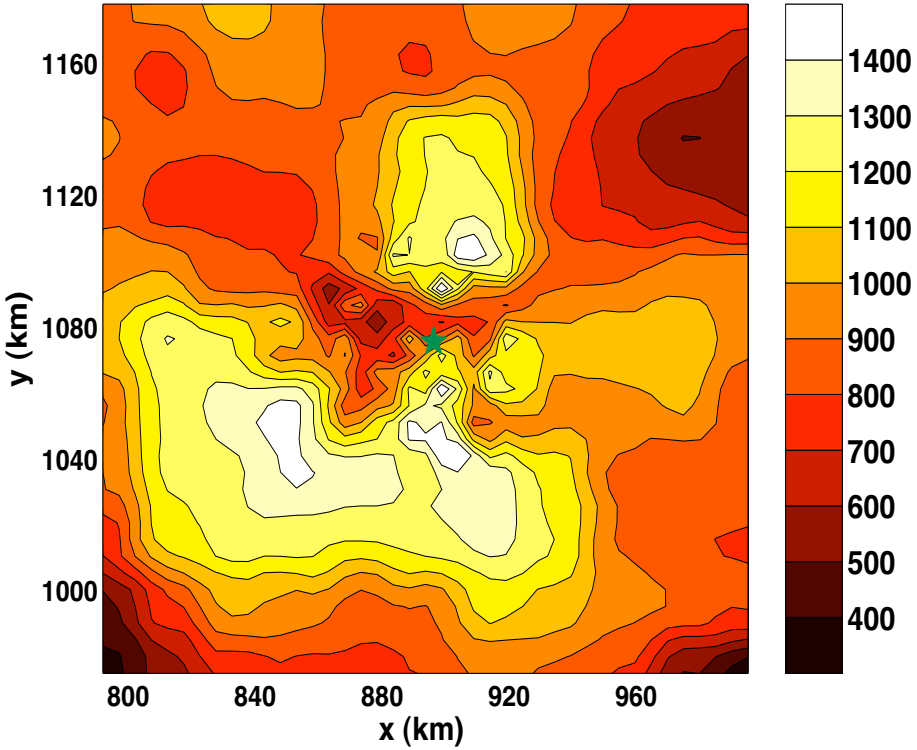

Fig. 3. Bedrock topography in the model domain (in m a.s.l., contour spacing 100 m). The green star indicates the location of the Dome Fuji drill site, north is towards the top right.

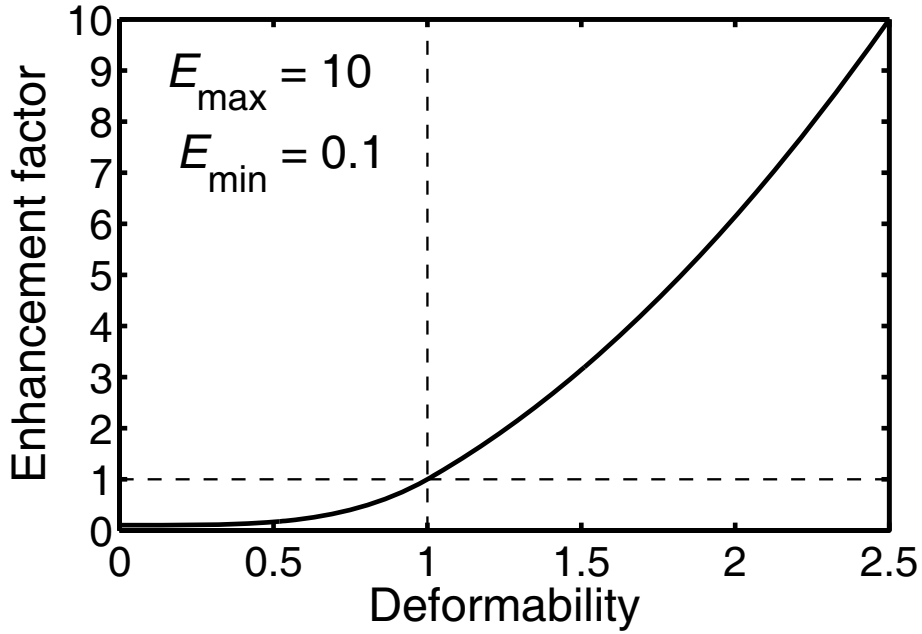

Fig. 4. Anisotropic enhancement factor $\hat{E}(\mathcal{A})$ as a function of the polycrystal deformability $\mathcal{A}$ according to Eq. (10), for E_{max}=10 and E_{min}=0.1.

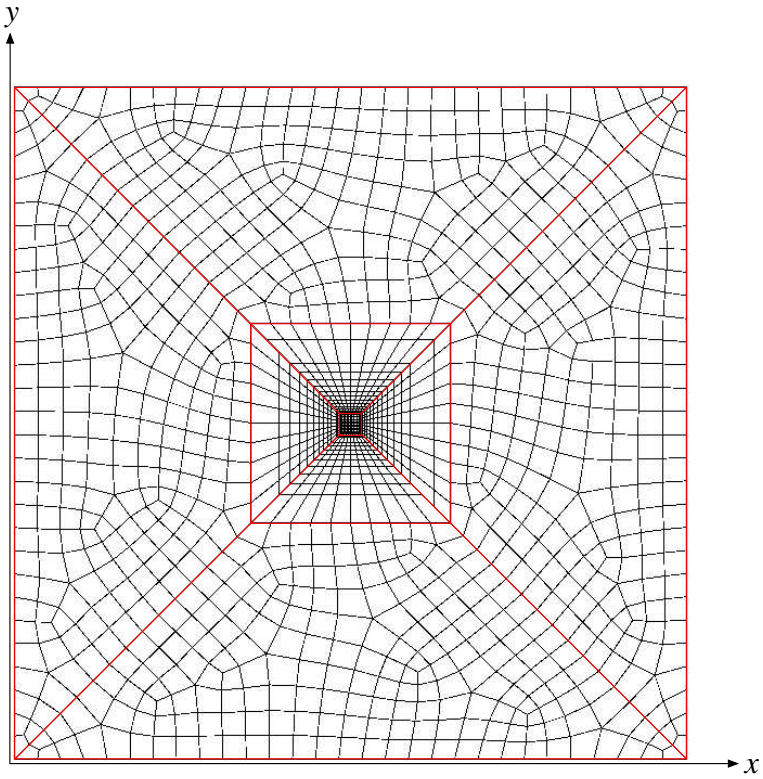

Fig. 5. Plan view of the finite-element mesh of the 203.092×203.092 km model domain (created with the pre-processing software Gambit). The inner 6×6 km and 60×60 km domains defined for creating the mesh (see main text) are marked as red squares.

TCD
3, 1–31, 2009

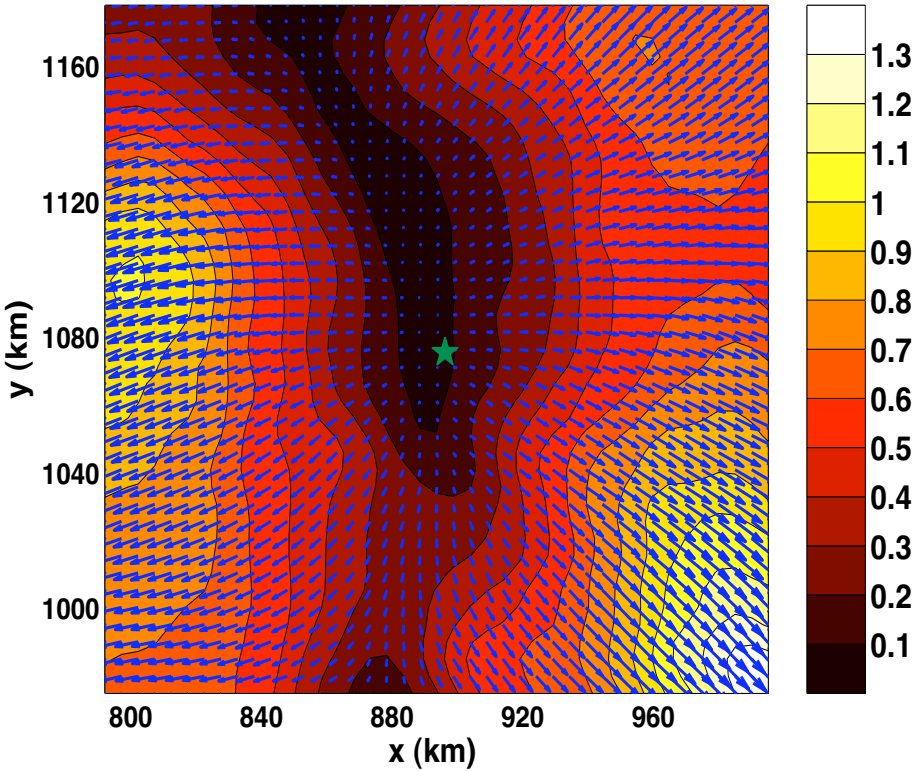

Fig. 6. Anisotropic steady-state simulation: Surface velocity (vectors) and speed (colour map and contours, in $\mathrm{m\,a^{-1}}$, contour spacing $0.1\,\mathrm{m\,a^{-1}}$). The green star indicates the location of the Dome Fuji drill site, north is towards the top right.

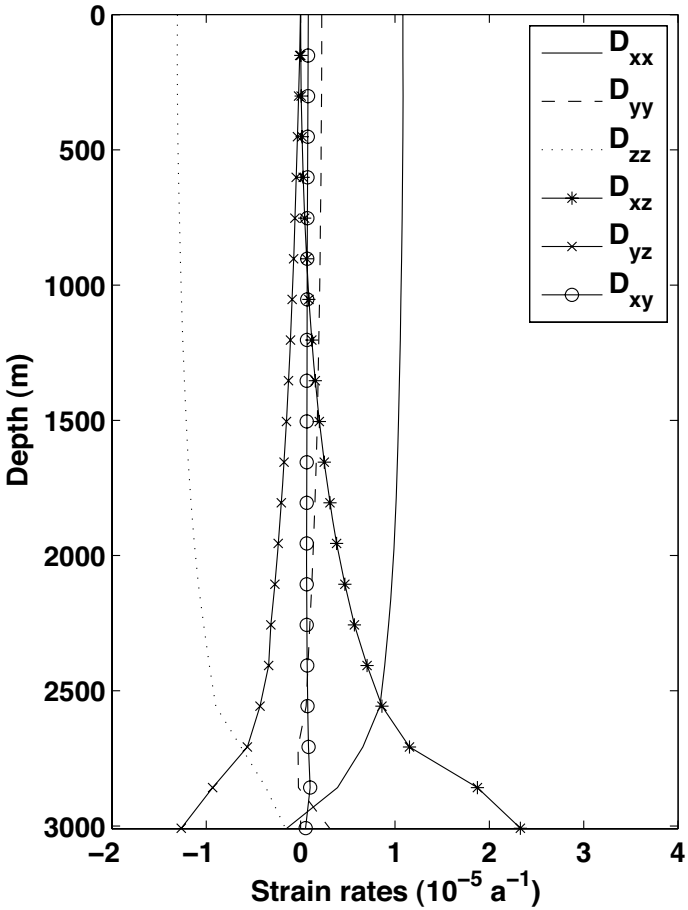

Fig. 7. Anisotropic steady-state simulation: Profiles of the components D_{xx}, D_{yy}, D_{zz}, D_{xy}, D_{yz} and D_{xz} of the strain-rate tensor D at the Dome Fuji drill site.

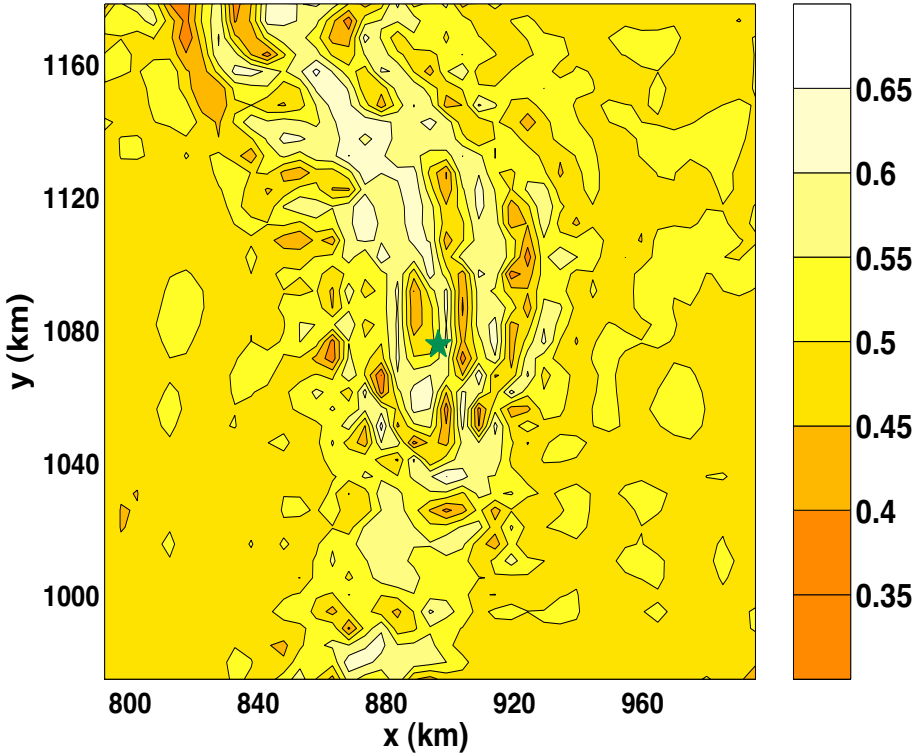

Fig. 8. Anisotropic steady-state simulation: Eigenvalue a_3 of the second-order orientation tensor $a^{(2)}$ at 95% depth (contour spacing 0.05). The green star indicates the location of the Dome Fuji drill site, north is towards the top right.

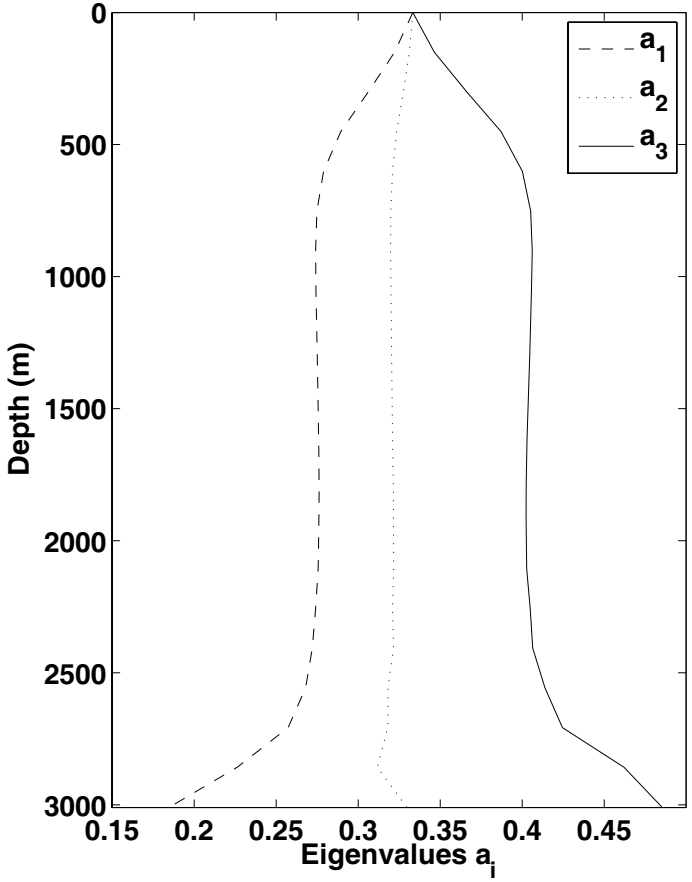

Fig. 9. Anisotropic steady-state simulation: Profiles of the eigenvalues a_1, a_2 and a_3 of the second-order orientation tensor $a^{(2)}$ at the Dome Fuji drill site.

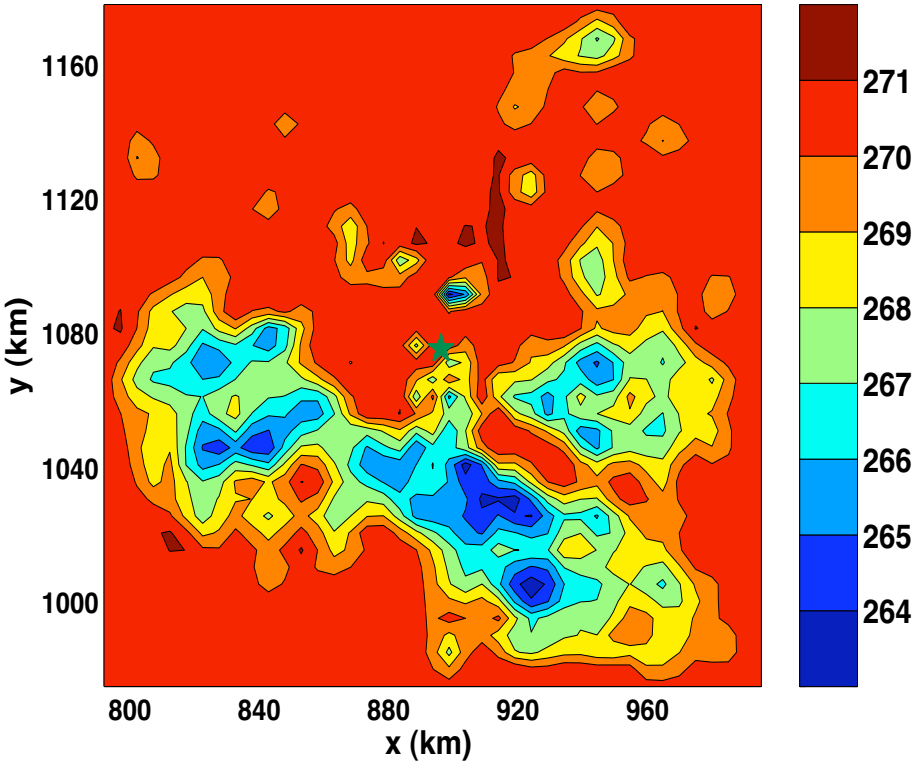

Fig. 10. Anisotropic steady-state simulation: Temperature at the ice base (in K, contour spacing 1 K). The green star indicates the location of the Dome Fuji drill site, north is towards the top right.

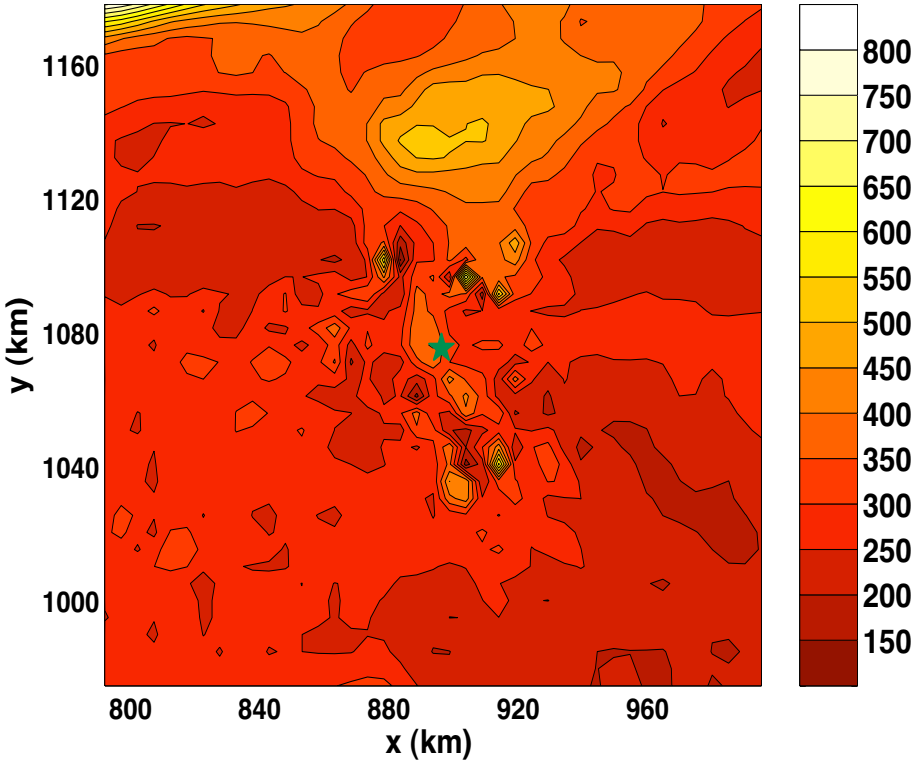

Fig. 11. Anisotropic steady-state simulation: Age at 95% depth (in ka, contour spacing 50 ka). The green star indicates the location of the Dome Fuji drill site, north is towards the top right.

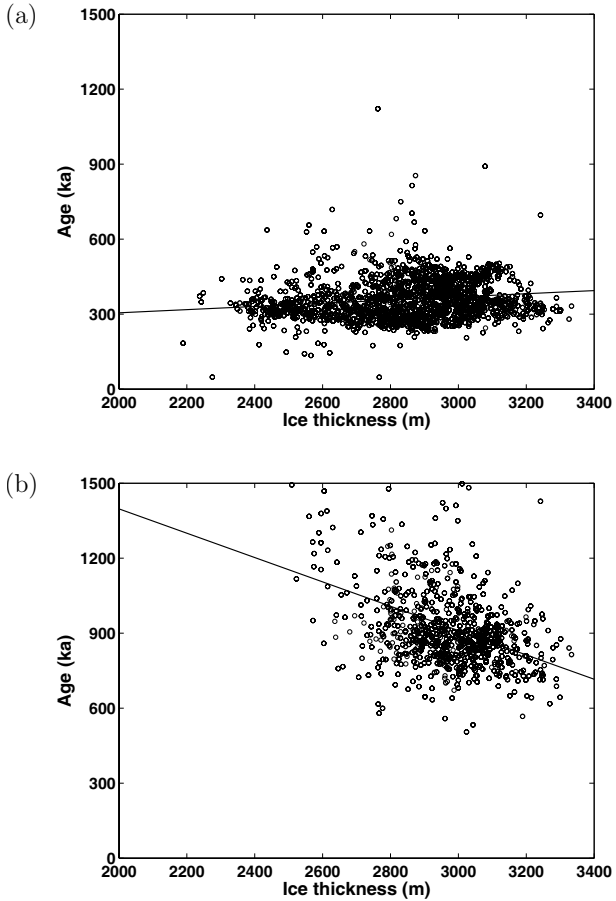

Fig. 12. Anisotropic steady-state run: **(a)** Age at 95% depth vs. ice thickness for all nodes of the finite-element mesh; linear regression line. **(b)** Basal age vs. ice thickness for all nodes of the finite-element mesh where the basal temperature is at the pressure melting point; linear regression line.

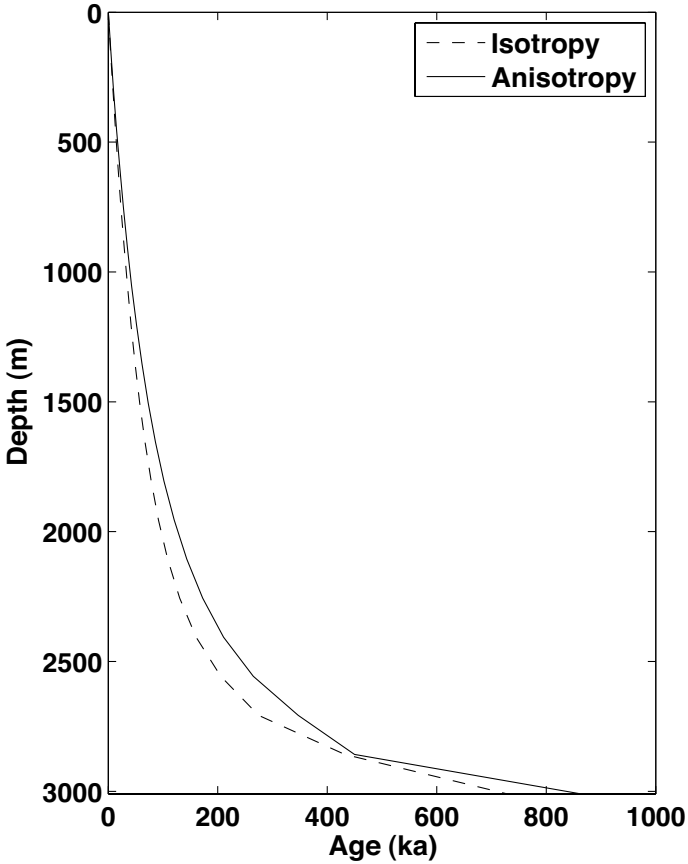

Fig. 13. Anisotropic and isotropic steady-state runs: Age profiles at the Dome Fuji drill site.

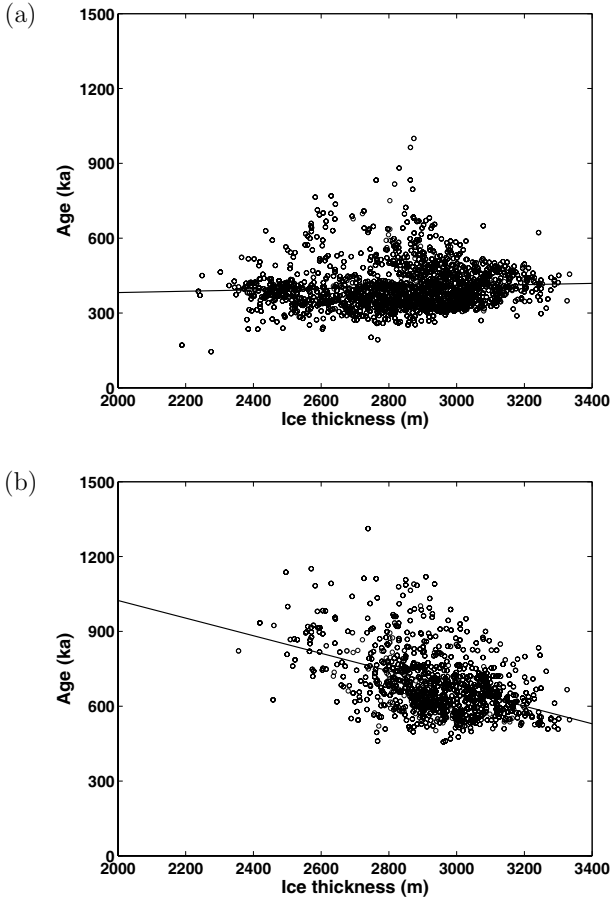

Fig. 14. Isotropic steady-state run: **(a)** Age at 95% depth vs. ice thickness for all nodes of the finite-element mesh; linear regression line. **(b)** Basal age vs. ice thickness for all nodes of the finite-element mesh where the basal temperature is at the pressure melting point; linear regression line.